Analysis of digital images into energy–angular momentum modes

Luis Edgar Vicent[1,†] and Kurt Bernardo Wolf[2,*]

[1]*Centro de Investigación en Ciencia Aplicada y Tecnología Avanzada, Unidad Altamira Instituto Politécnico Nacional, Altamira, Tamaulipas, 89600 México*

[2]*Instituto de Ciencias Físicas, Universidad Nacional Autónoma de México, Avenue Universidad s/n, Col. Chamilpa, Cuernavaca, Morelos, 62210 México*

**Corresponding author: bwolf@fis.unam.mx*

Received January 31, 2011; accepted February 10, 2011;
posted February 23, 2011 (Doc. ID 142063); published April 18, 2011

The measurement of continuous wave fields by a digital (pixellated) screen of sensors can be used to assess the quality of a beam by finding its formant modes. A generic continuous field $F(x,y)$ sampled at an $N\times N$ Cartesian grid of point sensors on a plane yields a matrix of values $F(q_x,q_y)$, where (q_x,q_y) are integer coordinates. When the approximate rotational symmetry of the input field is important, one may use the sampled Laguerre–Gauss functions, with radial and angular modes (n,m), to analyze them into their corresponding coefficients $F_{n,m}$ of energy and angular momentum (E-AM). The sampled E-AM modes span an N^2-dimensional space, but are not orthogonal—except for parity. In this paper, we propose the properly orthonormal "Laguerre–Kravchuk" discrete functions $\Lambda_{n,m}(q_x,q_y)$ as a convenient basis to analyze the sampled beams into their E-AM polar modes, and with them synthesize the input image exactly.

OCIS codes: 070.2025, 100.0100.

1. INTRODUCTION: LAGUERRE–GAUSS FUNCTIONS

Two-dimensional sensor arrays are customarily used to receive and analyze acoustic or phase-controlled optical beams, interpreting the data to resolve their formant modes. Assume the field is recorded by sampling its continuous complex function $F(x,y)$ on an $N\times N$ equally spaced square of points $(x,y)=s(q_x,q_y)$, for integer $q_x,q_y|_{-j}^{j}\in\square$—with $N=2j+1$ odd so that $(0,0)$ is the center point of the array $\square$—and an appropriate scale factor s to be determined. Out of this matrix of $N\times N$ data values $\{F(q_x,q_y)\}_{q_x,q_y\in\square}$, we want to find the coefficients of modes characterized by their number of nodal circles and radial lines. We should end up with N^2 coefficients out of which we could reconstruct the beam through a similar array of points acting as field emitters with controlled intensity and phase.

The set of Laguerre–Gauss eigenfunctions of the 2-dim quantum harmonic oscillator of energy $E_n=n+1$ $(n\in\{0,1,\ldots\})$ and angular momentum m are well known [1]:

$$\Phi^{\circ}_{n,m}(r,\theta):=\sqrt{\frac{\left(\frac{1}{2}(n-|m|)\right)!}{\pi\left(\frac{1}{2}(n+|m|)\right)!}}r^{|m|}e^{im\theta}e^{-r^2/2}L^{|m|}_{\frac{1}{2}(n-|m|)}(r^2),\quad(1)$$

where $L^{|m|}_{\nu}(r)$ is the associated Laguerre polynomial in the radius $r\geq 0$, and where the quantum numbers (n,m) have the integer ranges

$$n|_0^{\infty},\qquad m\in\{\pm n,\pm(n-2),\ldots,\pm 1\quad\text{or}\quad 0\}.\qquad(2)$$

We change coordinates to $x=r\cos\theta$, $y=r\sin\theta$, and the sampled values of Eq. (1) at the sensor points of a centered $N\times N$ square array with intersensor distance s, with $\sigma_m:=\mathrm{sign}m$, are written as

$$\Phi^{(s)}_{n,m}(q_x,q_y):=A_{n,m}(s)[s(q_x+\mathrm{i}\sigma_m q_y]^{|m|}\times e^{-\frac{1}{2}s^2(q_x^2+q_y^2)}L^{|m|}_{\frac{1}{2}(n-|m|)}(s^2(q_x^2+q_y^2)),\qquad(3)$$

where $A_{n,m}(s)$ are normalization factors in the complex N^2-dimensional vector space $\mathcal{V}$ of $N\times N$ matrices $(N=2j+1)$ F, G, whose inner product and norm are

$$(F,G)_{\square}:=\sum_{q_x,q_y\in\square}F(q_x,q_y)^*G(q_x,q_y),\qquad |F|:=\sqrt{(F,F)}.\quad(4)$$

Since there are only N^2 values provided by the sensor array, there cannot be more than N^2 linearly independent discrete functions $\Phi^{(s)}_{n,m}(q_x,q_y)$ among the (n,m) in Eq. (2) to form a basis for $\mathcal{V}$. We may conjecture that some subset bound from above by energy could provide them, but the number of states up to some E_n is $1+2+\cdots+n+1=\frac{1}{2}(n+1)(n+2)$, which does not fit the square N^2. One is faced thus with the dilemma of choosing among various subsets (n,m) of N^2 E-AM modes. Only parity $(q_x,q_y)\leftrightarrow(\pm q_x,\pm q_y)$ separates the states into four orthogonal subspaces. But generally, beyond the lowest n, the sampled Laguerre–Gauss functions of Eq. (3) form angles under Eq. (4) that become vanishingly small with growing n, so the computation of coefficients obtained from their dual basis becomes very unstable.

The orthonormal *Laguerre–Kravchuk* functions $\Lambda_{n,m}(q_x,q_y)$ are introduced in Section 2; they form a basis complete in $\mathcal{V}$ for indices (n,m) in a range $\diamond$ that we characterize in that section. This is a proper discrete E-AM basis in which we propose to perform the analysis and restore the original

signal on $N \times N$ arrays of sensor points. Some of their properties have been explored in [2–5]. In the case of one-dimensional arrays, the comparison between the use of sampled Hermite–Gauss versus Kravchuk functions was made in [6]; a similar comparison will be made here for the two-dimensional case of pixellated images. In Section 3 we settle the issue of the scale factor s in Eq. (3) by choosing the best fit of the sampled ground state $\Phi^{(s)}_{0,0}(q_x, q_y)$ to the lowest mode $\Lambda_{0,0}(q_x, q_y)$.

There are three analyses of an input field that we consider in Section 4: the expansion coefficients obtained by integration of the image with the Laguerre–Gauss functions, the sum of pixel data with the sampled functions, and the orthonormal expansion into Laguerre–Kravchuk functions. Since the sampled basis cannot be trusted for numerical reasons, in Section 5 we propose a successive projection algorithm that competes favorably with the inversion of their matrix. In Section 6 we conduct some numerical experiments on "discontinuous" and smooth input images, knowing that only the Laguerre–Kravchuk basis can restore the original digital images exactly. Some conclusions are offered in Section 7.

2. KRAVCHUK AND LAGUERRE–KRAVCHUK FUNCTIONS

The Laguerre–Kravchuk functions on the discrete array $q_x, q_y \in \square$ were built out of linear combinations of two Kravchuk functions of $q_x|^j_{-j}$ and of $q_y|^j_{-j}$ in [2]; the latter [7] are eigenfunctions of an N-point discrete oscillator model [8,9], and bases for irreducible representations of the Lie algebra $\mathsf{so}(3)$ [10,11]. Let us denote the generators of this algebra by J_1, J_2, and J_3; then, finite rotations are generated by their Lie exponentials, $\exp(\mathrm{i}\theta J_i)$, acting on N-vectors through $N \times N$ matrices. The matrix elements of $\exp(\mathrm{i}\theta J_2)$ are the well-known Wigner "little-d" functions of $d^j_{m,m'}\theta$, $N = 2j+1$ [10]. The overlap between the eigenfunctions of J_1 with *position* eigenvalue $q|^j_{-j}$, and the eigenfunctions of the orthogonal J_3 with displaced-*energy* eigenvalue $n-j$, or mode *number* $n|^{2j}_0$, is $d^j_{n-j,q}(\frac{1}{2}\pi)$: the finite oscillator wavefunctions [8]. They are expressible in terms of the square root of a binomial (discrete counterpart of the Gaussian), and a symmetric Kravchuk (*id.* for Hermite) polynomial [7,11–13]:

$$\Psi^j_n(q) := d^j_{n-j,q}(\tfrac{1}{2}\pi) \qquad n|^{2j}_0, \quad q|^j_j, \tag{5}$$

$$= \frac{(-1)^n}{2^j}\sqrt{\binom{2j}{n}\binom{2j}{j+q}}\,K_n\left(j+q;\tfrac{1}{2},2j\right), \tag{6}$$

$$K_n\left(j+q;\tfrac{1}{2},2j\right) = {}_2F_1(-n,-2j-q;-2j;2) = K_{j+q}\left(n;\tfrac{1}{2},2j\right). \tag{7}$$

The Kravchuk functions in Eq. (6) are real, orthonormal bases for $N = 2j+1$-dimensional vector spaces; under reflections $q \leftrightarrow -q$ their parity is $(-1)^n$. These have been used in 1-dim signal analyses [6,13], that we now extend to 2-dim images. For a two-dimensional array, the direct product of two Kravchuk bases yields the *Cartesian* modes:

$$\Psi^j_{n_x,n_y}(q_x, q_y) := \Psi^j_{n_x}(q_x)\Psi^j_{n_y}(q_y). \tag{8}$$

These are shown in Figure 1(a), in a rhomboidal arrangement indicated by $(n_x, n_y) \in \diamond$, of digital (pixellated) screens $(q_x, q_y) \in \square$. The total mode number is $n := n_x + n_y \in \{0, 1, \ldots, 4j\}$, and the energy is $E_n = n+1$ as before. These functions form a complete and orthonormal basis for $\mathcal{V}$, the N^2-dimensional space with the inner product from Eq. (4).

The Laguerre–Kravchuk E-AM basis $\Lambda^j_{n,m}(q_x, q_y)$ of $\mathcal{V}$ is now defined by *importing* [14] the relation between the continuous Hermite–Gauss and Laguerre–Gauss modes, which is given by a Wigner little-d function, and entails the linear combination of all modes with the same total mode number n. It is a unitary *gyration* [3] of the Cartesian basis of Eq. (8), defined by

$$\Lambda^j_{n,m}(q_x, q_y) := (-1)^{(|m|-m)/2} \sum_{n_x+n_y=n} (-\mathrm{i})^{n_y} d^{n/2}_{\frac{1}{2}(n_x-n_y),\frac{1}{2}m}(\tfrac{1}{2}\pi) \times \Psi^j_{n_x,n_y}(q_x, q_y). \tag{9}$$

They are orthonormal under the inner product of Eq. (4) of $\mathcal{V}$, the N^2-dimensional space of all digital screen functions,

$$(\Lambda^j_{n,m}, \Lambda^j_{n',m'})_\square = \delta_{n,n'}\delta_{m,m'}. \tag{10}$$

The set of Laguerre–Kravchuk functions in Eq. (9) is also complete in $\mathcal{V}$, and its indices (n, m) provide the basis for a dual space $\tilde{\mathcal{V}}$, whose inner product we denote by

$$(\tilde{F}, \tilde{G})_\diamond := \sum_{(n,m)\in\diamond} \tilde{F}^*_{n,m}\tilde{G}_{n,m}, \tag{11}$$

where the range of $(n, m) \in \diamond$ is determined by the range of $(n_x, n_y) \in \diamond$, and falls into two triangular subsets of indices

$$\text{lower}\nabla\text{: } n|^{2j}_0, \qquad m \in \{\pm 1 \quad \text{or} \quad 0, \ldots, \pm(n-2), \pm n\}, \tag{12}$$

$$\text{upper}\Delta\text{: } n|^{4j-2}_{2j}, \qquad m \in \{\pm 1 \quad \text{or} \quad 0, \ldots, \pm(4j-n-2), \pm(4j-n)\}, \tag{13}$$

that overlap for $n = 2j+1 = N$. Under this inner product, the Laguerre–Kravchuk states are also orthonormal:

$$(\Lambda^j(q_x, q_y), \Lambda^j(q'_x, q'_y))_\diamond = \delta_{q_x,q'_x}\delta_{q_y,q'_y}, \tag{14}$$

and thus provide the matrix transform kernel between $\mathcal{V}$ and $\tilde{\mathcal{V}}$.

The lower triangle in Eq. (12) contains the ground and lower modes, while the upper triangle in Eq. (13) contains highly oscillating functions. We show these E-AM modes in Figure 1(b). Since for $m \neq 0$ the angular factor in Eq. (9) is complex, it is convenient to plot the real functions:

$$\Lambda^j_{n,|m|,+}(q_x, q_y) = \frac{1}{\sqrt{2}}(\Lambda^j_{n,m}(q_x, q_y) + \Lambda^j_{n,-m}(q_x, q_y)),$$
$$\Lambda^j_{n,|m|,-}(q_x, q_y) = \frac{1}{\mathrm{i}\sqrt{2}}(\Lambda^j_{n,m}(q_x, q_y) - \Lambda^j_{n,-m}(q_x, q_y)). \tag{15}$$

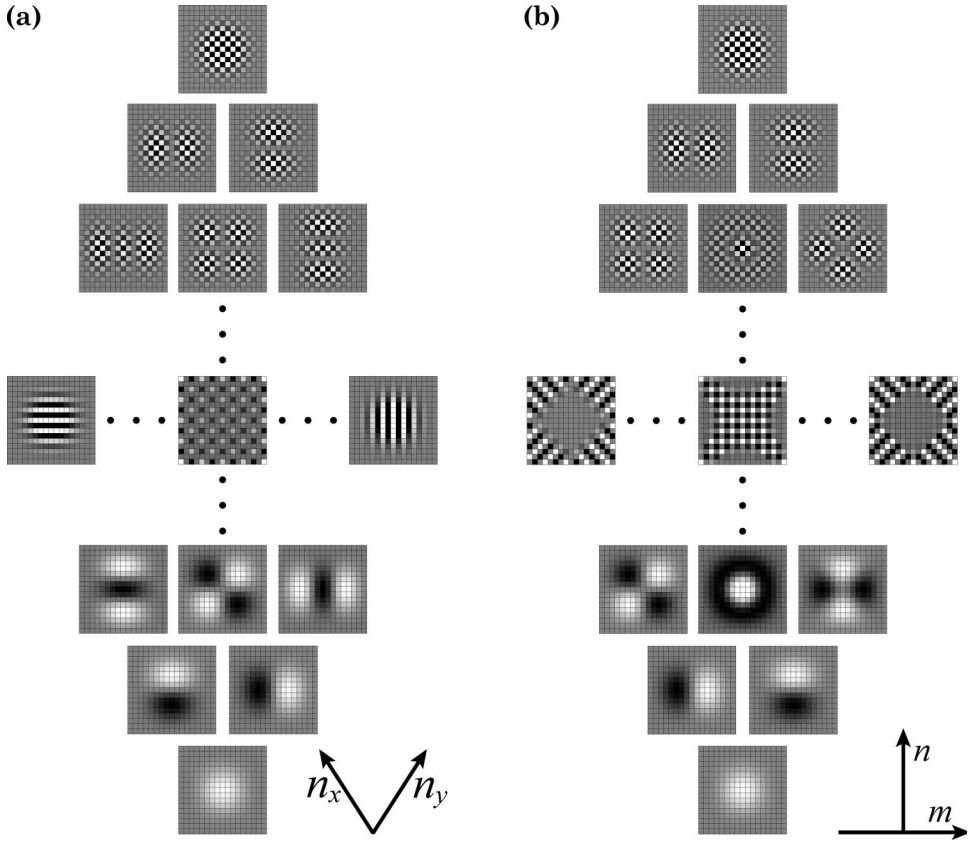

Fig. 1. (a) Two-dimensional Cartesian modes $\Psi^j_{n_x,n_y}(q_x,q_y)$, $(q_x,q_y)\in\square$, $n_x|_0^{2j}, n_y|_0^{2j}$, given by Eq. (8) for $j=8$ ($N=17$). At bottom is the ground state $(0,0)$ and at the top is the highest state $(2j,2j)$ that can be registered by the sensor array. (b) E-AM modes $\Lambda^j_{n,|m|,\pm}(q_x,q_y)$, $(n,m)\in\square$, obtained by the importation of symmetry [Eq. (9)] from linear combination of all states with total energy $n=n_x+n_y$, and angular momentum m, given by Eqs. (9) and (15). For $m<0$, we show the "sine" modes $\Lambda^j_{n,|m|,-}$, and for $m\geq 0$ the "cosine" modes $\Lambda^j_{n,|m|,+}$. At the bottom is the ground state $\Lambda^j_{n,|m|,+}=\Psi^j_{0,0}$ and at the top is the highest energy state $\Lambda^j_{4j-2,9,+}=\Psi^j_{2j,2j}$.

We note that the lower states $(m,n)\in\nabla$, including the ground state $(0,0)$, multiplied by a checkerboard of alternating signs, yield the higher states in Δ through reflection across their horizontal boundary, including the highest state $(4j,0)$. We have thus also resolved the dilemma posed in Section 1 regarding which sampled E-AM modes (n,m) we should include to match the N^2 data points of the sensor grid.

3. CALIBRATION OF SCALE FOR MODE EXPANSION

To calibrate the scale factor s in Eq. (3), we assume that the sensor array is fixed, and that the ground mode $\Phi_{0,0}(x,y)=\Psi_{0,0}(x,y)$ of the physical source of the beam can be centered; then it can be magnified or reduced to achieve a best match with the ground Laguerre–Kravchuk function $\Lambda^j_{0,0}(q_x,q_y)$ in Eq. (9). The input beam is sensed by the array as $\Phi^{(s)}_{0,0}(sq_x,sq_y)$, so we ask for the norm of their difference to be minimized:

$$D^j_0(s):=|\Lambda^j_{0,0}-\Phi^{(s)}_{0,0}|,\qquad D^j_0(\bar{s}):=\min_s D^j_0(s),\tag{16}$$

finding thus the optimal scale factor $\bar{s}$ for each array size $N=2j+1$. This minimum is unique because both functions have a single central positive bulge.

In [6] we compared the 1-dim sampled Hermite–Gauss ground states (for $j=7$ and 15) to find the optimal values of $\bar{s}$ for each j and showed graphically that this value does not change much with growing n; it only differs significantly for the highest values $n\approx 2j$. In two dimensions, the ground state is the product of two 1-dim ground states in the x and y directions, so the same value of $\bar{s}$ can be found here by scanning the $(q_x,0)$ or the $(0,q_y)$ lines. In that reference, for 31×31 sensor arrays ($j=15$) we determined that the minimum of the ground state difference, $D^{15}_0(s)$ occurs at $\bar{s}=0.258253$. With this value, we can compute all other differences $D^j_{n,m}(\bar{s}):=|\Lambda^j_{n,m}-\Phi^{(\bar{s})}_{n,m}|$, which grow slowly with n (as in the 1-dim case in [6]), up to the top of the rhombus of states in Figs. 1.

4. THREE EXPANSIONS IN E-AM MODES

A continuous image field, $\bar{F}(x,y)$, $(x,y)\in\Re^2$, can be synthesized from the infinite basis of continuous, normalized Laguerre–Gauss functions, $\Phi^{\circ}_{n,m}(r,\theta)\equiv\bar{\Phi}_{n,m}(x,y)$ in Eq. (1), with radial and angular mode coefficients $\{\bar{F}_{n,m}\}$ obtained through integration over $\Re^2$, as

$$\bar{F}(x,y)=\sum_{n=0}^{\infty}\sum_{m=-n}^{n}(2)\bar{F}_{n,m}\bar{\Phi}_{n,m}(x,y),\tag{17}$$

$$\bar{F}_{n,m}=\iint_{\Re^2}\mathrm{d}x\mathrm{d}y\bar{\Phi}_{n,m}(x,y)^*\bar{F}(x,y),\tag{18}$$

where the sum over m is understood to be in steps of 2, and by overlines we identify the continuous field and its integral E-AM coefficients. These integral coefficients will be

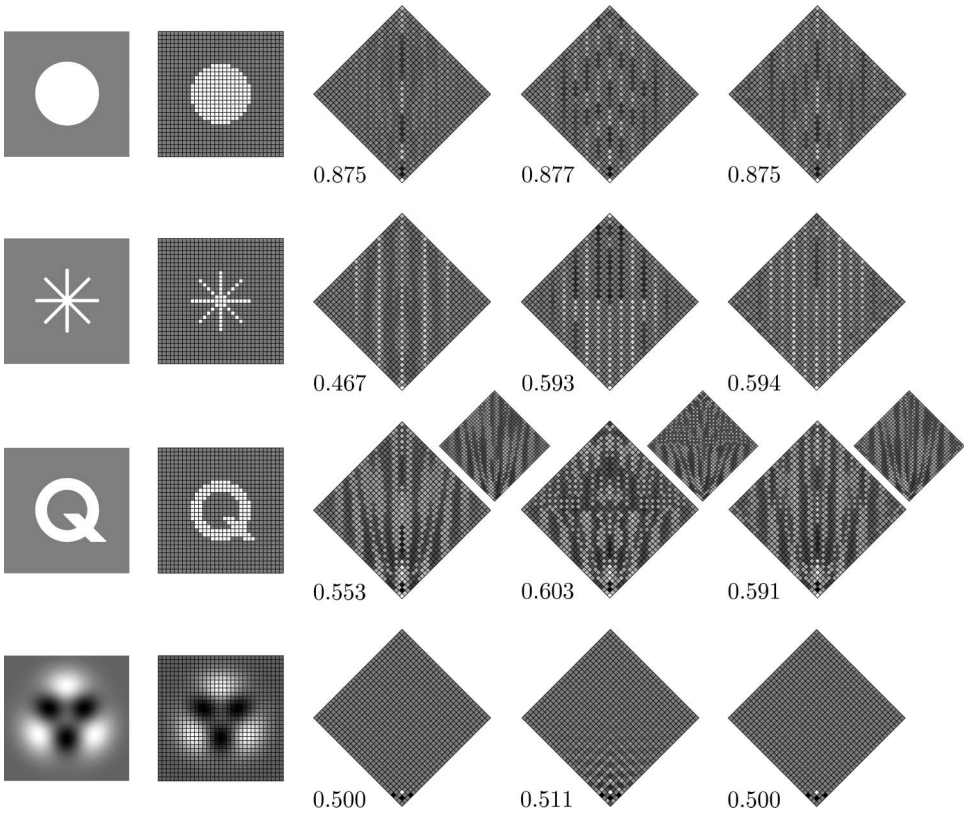

Fig. 2. First and second columns, four continuous fields $F(q_x, q_y)$ and their sampled digital images on a 31×31 ($j = 15$) grid $(q_x, q_y) \in \square$: a circular drum function $\bar{F}^{\circ}(r, \theta) = 1$ for $r \le 7.5$ and zero otherwise; a rosetta with eight spokes of 1 pixel width; a letter Q, whose "tail" partially breaks rotational symmetry; the smooth field $\bar{F} = -\Phi^{\circ}_{2,0} - \Phi^{\circ}_{3,3} - \Phi^{\circ}_{3,-3} + \Phi^{\circ}_{4,0}$. Third column, integral E-AM coefficients $\bar{F}_{n,m}$ of the images in the first column, obtained from the integration in Eq. (18), for $(n, m) \in \diamond$. The numbers under each rhombus give the absolute maximum of the pixel values; the gray tones were chosen to highlight the values near zero as explained in the text. The Q image has complex coefficients; the larger rhombus shows the real part and the smaller one the imaginary part, both scaled by their common absolute maximum. Fourth column, Laguerre–Kravchuk E-AM coefficients $F^K_{n,m}$ in Eq. (23), $(n, m) \in \diamond$, of the digital images in the second column. Fifth column, sampled Laguerre–Gauss expansion coefficients $f_{n,m}$ obtained from Eq. (25), $(n, m) \in \diamond$, of the same digital images.

compared with their approximations obtained for the set of N^2 data obtained from the digital screen of sensors.

To implement such algorithms on $N^2 \times N^2$ matrices and N^2 vectors, we require a numeration convention to assign a single index q to the pair (q_x, q_y), to be denoted by $q|_1^{N^2} \leftrightarrow (q_x, q_y) \in \square$; and another convention for the E-AM pair of indices, $\nu|_1^{N^2} \leftrightarrow (n, m) \in \diamond$. These are established and detailed in Appendix A.

The synthesis and analysis of a digital image vector $\{F_q\} \leftrightarrow \{F(q_x, q_y)\} \in \mathcal{V}$ in terms of a matrix formed by the nonorthogonal basis of sampled Laguerre–Gauss functions, $\Phi^{(\bar{s})}_{n,m}$ in Eq. (3), with coefficients $\{F^L_\nu\} \leftrightarrow \{F^L_{(n,m)}\}$, is

$$F_q = \sum_\nu L_{q,\nu} F^L_\nu \leftrightarrow F(q_x, q_y) = \sum_{n,m \in \diamond} L_{(q_x,q_y),(n,m)} F^L_{n,m}, \tag{19}$$

$$F^L_\nu = \sum_q (L^{-1})_{\nu,q} F_q \leftrightarrow F^L_{n,m} = \sum_{q_x,q_y \in \square} (L^{-1})_{(n,m),(q_x,q_y)} F(q_x, q_y), \tag{20}$$

$$\text{where } L_{q,\nu} \leftrightarrow L_{(q_x,q_y),(n,m)} := \Phi^{(\bar{s})}_{n,m}(q_x, q_y). \tag{21}$$

Since the $N^2 \times N^2$ $L = \|L_{k,k'}\|$ contains rows of sampled Laguerre–Gauss functions that form very small angles among themselves, its determinant is very near to zero, as was noted in the 1-dim case studied in [6], where, for $N = 31$, $\det L \approx 2.33 \times 10^{-41}$.

On the other hand, the finite digital image may be readily expanded in terms of the orthonormal and complete Laguerre–Kravchuk functions in Eq. (9), $\Lambda^j_\nu(q) \leftrightarrow \Lambda^j_{n,m}(q_x, q_y)$, with the same assignments $q := (q_x, q_y)$ and $\nu := (n, m)$ as above. It reads

$$F_q = \sum_\nu K_{q,\nu} F^K_\nu \leftrightarrow F(q_x, q_y) = \sum_{n,m \in \diamond} K_{(q_x,q_y),(n,m)} F^K_{n,m}, \tag{22}$$

$$F^K_\nu = \sum_q K^*_{\nu,q} F_q \leftrightarrow F^K_{n,m} = \sum_{q_x,q_y \in \square} K^*_{(q_x,q_y),(n,m)} F(q_x, q_y), \tag{23}$$

$$\text{where } K_{q,\nu} \leftrightarrow K_{(q_x,q_y),(n,m)} := \Lambda_{n,m}(q_x, q_y). \tag{24}$$

The determinant of the matrix $K = \|K_{k,k'}\|$ is 1.

We should not discard the sampled Laguerre–Gauss functions for not forming an orthonormal basis, with an inverse transform matrix from Eq. (21) that is unstable. As in [6], this basis can used with a different algorithm that we now proceed to describe.

5. SUCCESSIVE PROJECTION ALGORITHM

Understanding that the sampled basis does not have a good dual basis, we give an algorithm that successively projects out the lowest and then the higher modes. First one asks for the overlap of the signal with the optimally sampled

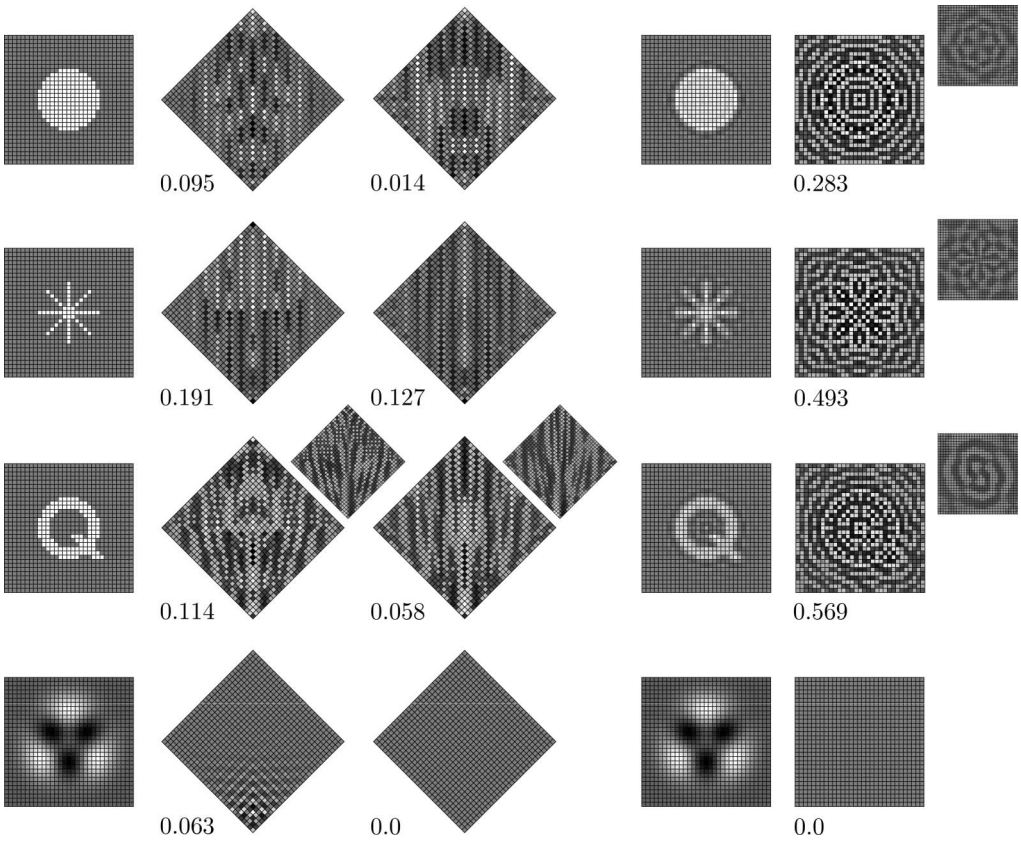

Fig. 3. First column, input digital images from the second column of Fig. 2. Second column, differences between the integral and Laguerre–Kravchuk E-AM coefficients, $\bar{F}_{n,m} - F^{K}_{n,m}$ over $(n,m) \in \diamond$; the numbers under each rhombus give their absolute maximum; for the Q image, real and imaginary parts are shown as in the previous figure. With these coefficients, the synthesis of the input image will be exact. Third column, differences between the integral and the sampled Laguerre–Gauss E-AM coefficients, $\bar{F}_{n,m} - f_{n,m}$; the absolute maximum values are indicated as in the previous column. Fourth column, reconstruction of the input image using the sampled Laguerre–Gauss E-AM coefficients found from the successive projection algorithm in Eq. (25), $\sum_{n,m} f_{n,m} \Phi^{(\bar{s})}_{n,m}(q_x, q_y)$, $(q_x, q_y) \in \square$. There appear Gibbs-like oscillations on the sharp boundaries. Fifth column, remanents $\Delta^{(N^2)}(q_x, q_y)$ in Eq. (26) of the differences between the input image and its reconstruction of the previous column; again, absolute maxima are indicated, and real and imaginary parts occupy the large and small squares, respectively. It is evident that they are rather large.

ground state $\Phi^{(\bar{s})}_0(q)$, and subtracts this component from the signal; the remaining signal (now with no $\Phi^{(\bar{s})}_0$ component) is then overlapped with the next higher sampled state, which is again subtracted from the signal (having now no $\Phi^{(\bar{s})}_\nu$, $\nu = 0, 1$ components); and so successively. This algorithm builds a sequence of difference vectors:

$$\begin{aligned} &\Delta^{(\nu+1)}(q) = \Delta^{(\nu)}(q) - f_\nu \Phi^{(\bar{s})}_\nu(q), \\ &\Delta^{(0)}(q) := F(q), \qquad f_\nu := (\Delta^{(\nu)}, \Phi^{(\bar{s})}_\nu)_N. \end{aligned} \tag{25}$$

In this way, the signal is analyzed into the sampled basis with coefficients $\{f_\nu\}_{\nu=0}^{N^2-1}$ as

$$\begin{aligned} F(q) = &f_0 \Phi^{(\bar{s})}_0(q) + f_1 \Phi^{(\bar{s})}_1(q) + \cdots + f_{N^2-1} \Phi^{(\bar{s})}_{N^2-1}(q) \\ &+ \Delta^{(N^2)}(q), \end{aligned} \tag{26}$$

where we note that there is no guarantee that the norm of the remanent vector $\Delta^{(N^2)}(q)$ in Eq. (26) be zero. This algorithm permits a fair approximation to the integral coefficients of the continuous signal, but may fail to reconstruct the input signal exactly.

The succesive projection algorithm must use an appropriate numbering scheme to define $\nu := (n,m)$ in the rhombus of Fig. 1(b). This is important because it implies that, beyond the ground state $(0,0) = 0$, the more likely modes should have the lowest numbers. In Appendix A, we decided to successively project out states of increasing energy $0 \le n \le 4j$ and, at each level, states of increasing angular momentum.

6. EXAMPLES OF ANALYSES AND SYNTHESES

To appreciate the relative merits afforded by the finite Laguerre–Kravchuk basis versus the sampled Laguerre–Gauss functions, in Fig. 2 we confront the integral Laguerre–Gauss coefficients $\bar{F}_{n,m}$ obtained from Eq. (18) with the Laguerre–Kravchuk coefficients $F^{K}_{n,m}$ in Eq. (23), and with the coefficients $f_{n,m}$ determined from the sampled functions in Eq. (25) over the rhombus $(n,m) \in \diamond$. Comparison of the discrete coefficient sets with the integral ones, and the remanent of the images reconstructed from the sampled set are shown in Fig. 3.

Symmetry considerations are useful to interpret coefficient patterns. Indicating by $X_{n,m}(q_x, q_y)$ any of the three function sets, $\Phi^{\circ}_{n,m}(x,y)$ in Eq. (1), $\Phi^{(\bar{s})}_{(n,m)}(q_x, q_y)$ in Eq. (3), or $\Lambda^{j}_{n,m}(q_x, q_y)$ in Eq. (9), their common properties under complex conjugation and reflection across the screen coordinate axes are

$$X_{n,m}(q_x, q_y) = X_{n,-m}(q_x, q_y)^*, \tag{27}$$

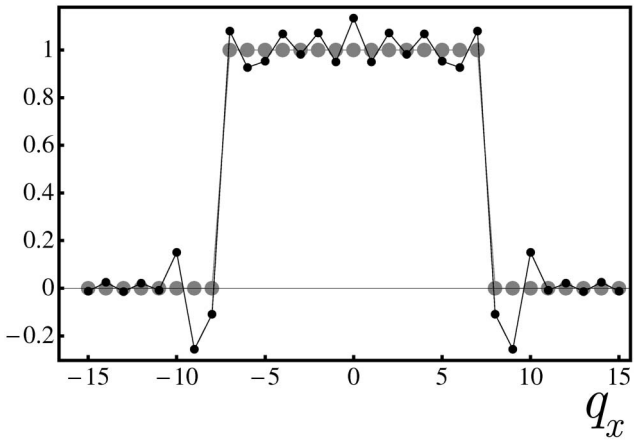

Fig. 4. Reconstruction [Eq. (26)] of the central pixel line of the drum function with the sampled Laguerre–Gauss E-AM coefficients (small black dots), compared with the original signal (large gray dots), which is obtained with the Laguerre–Kravchuk analysis. There is an overshoot of ≈28% when the sampled function coefficients are used.

$$= (-1)^m X_{n,-m}(-q_x, q_y) = X_{n,-m}(q_x, -q_y). \tag{28}$$

These relations are the same as for Fourier series expansions in $e^{\mathrm{i}m\theta}$, but keeping in mind that, due to Eqs. (2), (12), and (13), odd or even m occur only in rows of odd or even n, respectively.

In order to display the coefficients in any of the three expansions (indicated generically by $\{\xi_{n,m}\}_{n,m\in\diamond}$), we rescale and shift their values so that $X := \max_{n,m}|\xi_{n,m}|$ corresponds to 1 (white) and $-X$ to −1 (black). Then, to highlight the small values $\xi_{n,m} \approx 0$ of most coefficients, we magnify them through the map $\xi' := \xi^{1/4}$ when $\xi > 0$, and $\xi' := -|\xi|^{1/4}$ when $\xi < 0$; thus, the midgrays exaggerate the small differences from zero.

In any of the three basis expansions, real images $F(q_x, q_y)$ will have E-AM coefficients related by $\xi_{n,m} = \xi^*_{n,-m}$, and pure imaginary images, $\xi_{n,m} = -\xi^*_{n,-m}$. Images symmetric under reflection $q_x \leftrightarrow -q_x$ will exhibit E-AM coefficients $\xi_{n,m} = (-1)^m \xi_{n,-m}$, while those symmetric under $q_y \leftrightarrow -q_y$ have $\xi_{n,m} = \xi_{n,-m}$. Hence, the real images symmetric under both x and y reflections —such as the drum and rosetta in Figs. 2 and 3—will have coefficients $\xi_{n,m}$ that are real, and zero for all odd m. The Q image breaks the symmetry and thus acquires an imaginary part. Finally, having the E-AM coefficients $\xi_{n,m}$ of an image $F(q_x, q_y)$ allows us to rotate the image by an angle α through multiplying these coefficients by the phases $\exp(\mathrm{i}m\alpha)$ [5].

In Fig. 2 we note the difference between the E-AM mode content of the first three "discontinuous" images (drum, rosetta, and Q), and the analysis of the smooth function in the bottom row. The drum and rosetta are real and symmetric under x and y reflections, so their coefficients $\{F_{n,m}\}$ are real, and those of odd m (in rows of odd n) must be zero. In the Q image, this symmetry is broken and the coefficients become complex. In the drum image, the $m = 0$ coefficients are most prominent, but other even m are not strictly zero; the n line is essentially the expansion of a step function into Laguerre coefficients. In the rosetta image, the angular modes $m = \pm 8$ are most prominent, with an admixture of $m = 0, \pm 4, \pm 12, \ldots$ modes confined to lower energies. In the last row, the image is smooth and the four formant modes $(n, m) = (2, 0), (3, \pm 3)$ and $(4, 0)$ stand out clearly, with no noticeable difference between the integral and digital bases. All three coefficient sets resemble each other in the lowest modes, but, for the discontinuous cases, the highest modes are considerably different.

Particularly relevant as a criterion for comparison between the Laguerre–Kravchuk and sampled Laguerre–Gauss syntheses is the analysis of Fig. 3. As was the case of one dimension [6], the sampled Laguerre–Gauss coefficients $f_{n,m}$ in Eq. (25) show smaller departures from the "true" integral coefficients. However, they cannot reconstruct the original image exactly, except when it is very smooth, as in the bottom line of that figure. In the last two columns, where we show the approximation and remanents $\Delta^{(N^2)}(q_x, q_y)$ of Eq. (26), we see a Gibbs-like phenomenon at the edges of "discontinuity" of the original image. This is to be expected, as was the case for 1-dim signals in [6], Fig. 9. To further the comparison, in Fig. 4 we show the $q_y = 0$ line of values of the reconstructed image of the drum in the previous Fig. 3. The oscillations are not small, but (for $j = 15$) display an over- and undershoot of ≈28% of the discontinuities in the drum, and larger ones in the rosetta and Q syntheses. In contrast, the Laguerre–Kravchuk synthesis will reconstruct the original image exactly.

7. CONCLUSIONS

The context of this work is the approximation by finite to continuous models of optics. Finite Fourier analysis of digital images is well understood and widely used. Analysis in terms of modes of E-AM serves for beam quality control by square (or rectangular) CCD arrays of sensors. We here analyzed finite signals into their formant E-AM modes of Laguerre–Kravchuk functions; these are eigenfunctions of Hamilton equations [8] that translate the classical oscillator dynamics to finite systems [2,4]. They have attractive group-theoretical properties that are well known in the context of quantum angular momentum and the rotation group [10].

Adapting this mathematical apparatus for image analysis and processing requires a comparison with the more traditional use of sampled Laguerre–Gauss functions, where usually only the lowest energy mode content of a beam is of interest. Indeed, sampled Laguerre–Gauss functions with E-AM coefficients found with the successive projection algorithm in Eq. (25) approximate better image fields that are smooth, containing only a few of the lowest modes. Where our group-theoretical treatment has an edge is in the reconstruction of images that present contrasted detail, because it will be exact.

It may be that the arrangement of CCD sensors in Cartesian arrays is not optimal when the purpose is to analyze a beam into its E-AM components. The alternative would be an array with concentric circles of sensors, such as proposed in [15,16], where on radii $r = 0, 1, 2, \ldots, 2j$ are placed $1, 3, 5, \ldots, 4j + 1$ equidistant sensors. Such arrays have also $N^2 = (2j + 1)^2$ sensors, and are favored by the use of orthogonal and complete bases of functions described in those references. The functions turn out to be special Clebsch–Gordan coefficients [15] given by Hahn polynomials. Exploring the relative merit of image analysis with these and with sampled Laguerre–Gauss functions is a natural sequel to the present work.

APPENDIX A: NUMERATION PIXELS AND MODES

In the successive approximation algorithm given in Section 5, the assignment $q := (q_x, q_y)$, $q|_1^{N^2}$ to find the expansion coefficients in Eq. (25) from the inner product in Eq. (4) is actually immaterial; it could be $q = N(j + q_x) + j + q_y + 1$ to sum over columns, or $q = j + q_x + N(j + q_y) + 1$ to sum over rows.

On the other hand, the assignment we use for $\nu := (n, m)$ in the successive projection algorithm follows from the assumption that the lower values of the index ν will be the more prominent in the images to be analyzed, namely, those of lowest energy and lowest angular momenta. In Section 5, we counted the index $\nu|_0^{N^2}$ as illustrated below for $N = 5$ (namely $j = 2$), where $n|_0^8$ and where, for each energy, the angular momenta $m|_{-n}^{n}$ are spaced by 2:

$n = 8$					25					
7				23		24				
6			21		20		22			
5		18		16		17		19		
4	14		12		11		13		15	
3		9		7		8		10		
2			5		4		6			
1				2		3				
0					1					
$m = -5$	-4	-3	-2	-1	0	1	2	3	4	5

The index assignment algorithm first proceeds from $n = 0$ up to $2j$ (in $\nabla \subset \diamond$); when n is even, then the angular momenta are ordered by $m_i = (-1)^i 2\lfloor \frac{1}{2} i \rfloor$ for $i = 1, 2, \ldots, n + 1$ (where $\lfloor x \rfloor$ is the integer part of x); when n is odd, then the m are ordered by $m_i = (-1)^{i+1} 2\lfloor \frac{1}{2}(i - 1) \rfloor + 1$, also for $i = 1, 2, \ldots, n + 1$. For mode numbers from $n = 2j + 1$ up to $4j$ (in $\Delta \subset \diamond$), the index i above ranges from 1 to $4j - n + 1$.

ACKNOWLEDGMENTS

We thank the support of the Óptica Matemática projects DGAPA-UNAM IN-105008 and SEP-CONACYT 79899.

†This article is dedicated to the memory of Luis Edgar Vincent, the heart and soul of our little clan.

REFERENCES

1. A. Frank and P. Van Isacker, *Algebraic Methods in Molecular and Nuclear Structure Physics* (Wiley, 1998), Section 1.1.
2. N. M. Atakishiyev, G. S. Pogosyan, L. E. Vicent, and K. B. Wolf, "Finite two-dimensional oscillator. I: The Cartesian model," J. Phys. A **34**, 9381–9398 (2001).
3. K. B. Wolf and T. Alieva, "Rotation and gyration of finite two-dimensional modes," J. Opt. Soc. Am. A **25**, 365–370 (2008).
4. K. B. Wolf, "Discrete systems and signals on phase space," Appl. Math. Inf. Sci. **4**, 141–181 (2010).
5. L. E. Vicent, "Unitary rotation of square pixellated images," Appl. Math. Comput. **211**, 111–117 (2009).
6. K. B. Wolf, "Mode analysis and signal restoration with Kravchuk functions," J. Opt. Soc. Am. A **26**, 509–516 (2009).
7. M. Krawtchouk, "Sur une généralization des polinômes d'Hermite," C. R. Acad. Sci. Paris Ser. IV **189**, 620–622 (1929).
8. N. M. Atakishiyev, G. S. Pogosyan, and K. B. Wolf, "Finite models of the oscillator," Phys. Part. Atomic Nuclei **36**, 521–555 (2005).
9. N. M. Atakishiyev, G. S. Pogosyan, and K. B. Wolf, "Contraction of the finite one-dimensional oscillator," Int. J. Mod. Phys. A **18**, 317–327 (2003).
10. L. C. Biedenharn and J. D. Louck, "Angular momentum in quantum mechanics," *Encyclopedia of Mathematics and its Applications*, G.-C. Rota, ed. (Addison-Wesley, 1981), Section 3.6.
11. N. M. Atakishiyev and S. K. Suslov, "Difference analogs of the harmonic oscillator," Theor. Math. Phys. **85**, 1055–1062 (1990).
12. N. M. Atakishiyev and K. B. Wolf, "Fractional Fourier-Kravchuk transform," J. Opt. Soc. Am. A **14**, 1467–1477 (1997).
13. N. M. Atakishiyev, L. E. Vicent, and K. B. Wolf, "Continuous vs. discrete fractional Fourier transforms," J. Comput. Appl. Math. **107**, 73–95 (1999).
14. L. Barker, Ç. Candan, T. Hakioğlu, A. Kutay, and H. M. Ozaktas, "The discrete harmonic oscillator, Harper's equation, and the discrete fractional Fourier transform," J. Phys. A **33**, 2209–2222 (2000).
15. N. M. Atakishiyev, G. S. Pogosyan, L. E. Vicent, and K. B. Wolf, "Finite two-dimensional oscillator. II: The radial model," J. Phys. A **34**, 9399–9415 (2001).
16. N. M. Atakishiyev, G. S. Pogosyan, and K. B. Wolf, "Contraction of the finite radial oscillator," Int. J. Mod. Phys. A **18**, 329–341 (2003).